coatings

MDPI

Key Parameters and Optimal Design of a Split Induction Coil for T-Shaped Pipe Brazing

Zhenlin Zhang [1,2], Ziheng Yang [1,2], Pu Xie [3], Yue Zhao [4,5,*], Jiguo Shan [4,5], Yan Liu [1,2,*], Aiping Wu [4,5], Sida Ma [6], Lei Zhang [7] and Hui Chen [1,2,*]

1 School of Materials Science and Engineering, Southwest Jiaotong University, Chengdu 610031, China; zzl21@swjtu.edu.cn (Z.Z.)
2 Key Laboratory of Advanced Technologies of Materials, Ministry of Education, Chengdu 610031, China
3 Department of Aeronutics and Astronautics, Stanford University, Stanford, CA 94305, USA
4 Department of Mechanical Engineering, Tsinghua University, Beijing 100084, China
5 Key Laboratory for Advanced Materials Processing Technology, Ministry of Education, Beijing 100084, China
6 Beijing Institute of Radio Measurement, Beijing 100009, China
7 State Key Laboratory of Advanced Brazing Filler Metals and Technology, Zhengzhou Research Institute of Mechanical Engineering Co., Ltd., Zhengzhou 450001, China
* Correspondence: zhao-yue@tsinghua.edu.cn (Y.Z.); liuyanzt@163.com (Y.L.); xnrpt@swjtu.edu.cn (H.C.)

Abstract: The heat exchanger made up of several T-shaped joints is a critical component in energy equipment. A split induction coil was designed for T-shaped aluminum pipe brazing, and the Taguchi method was combined with multi-physical simulation to solve the multi-factor optimization of the split coil. The results showed that the multi-physical simulation model had high precision. The melting of filler metal was almost consistent with the spatial distribution of the temperature field, and the average simulation error was approximately 5.753 °C. The optimal coil parameters were obtained with a turn number of 3.5, a turn space of 7 mm, a heating distance of 15.6 mm, a coil diameter of 8 mm, and a coil length of 9 mm. Three well-formed T-shaped joints could be obtained at one time via the optimal split coil. During the induction brazing, the skin effects and the proximity effects induced a high magnetic field intensity around the joint, which had a significant relationship with the coil length and coil diameter. The high magnetic field intensity promoted a high eddy current density in this place, and as a result, the high Joule heat could be generated around the joint. In addition, the significant decrease in the heating rate at high temperatures promoted the homogenization of the temperature and the melting and filling of the filler metal as well as avoided local overheating.

Keywords: induction brazing; numerical simulation; Taguchi method; split coil; temperature field

1. Introduction

The heat exchanger is a device that is used for the transfer of internal thermal energy between two or more fluids available at different temperatures, and it plays an important role in energy efficiency and physical size of the refrigeration and air conditioning system [1,2]. Figure 1 shows one type of heat exchanger morphology. One of the most important issues in the manufacturing of the heat exchanger is the joining of the header tubes and flat tubes, which are its key heating transferring components. Furthermore, tubes and fins belong to thermal conductive adhesive joining, and when the temperature reaches 200 °C or more, the joint loses efficacy. Therefore, brazing without using the furnace can be used to join the flat tube and header pipe of the heat exchanger in the air conditioner, and the distribution of temperature is very essential. In addition, the deformation should be controlled in the length direction during brazing, or it will produce a force that is perpendicular to the header pipe, thus reducing the lifetime of the brazing joint.
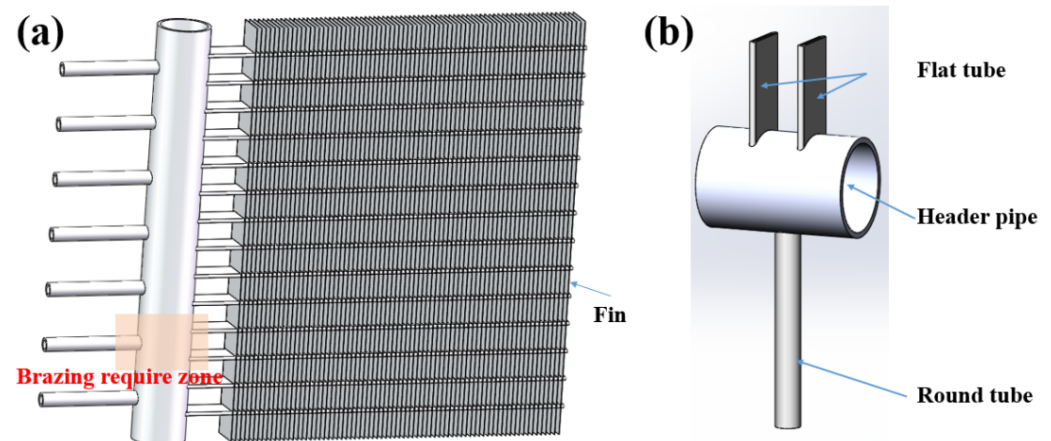
Figure 1. Heat exchanger: (**a**) morphology and (**b**) brazing requirements among header pipe and tubes.

Brazing without using furnace technologies includes mainly torch brazing [3], resistance brazing [4], dip brazing, ultrasonic brazing [5], and induction brazing [6]. Because of its reliable control, nonnecessity of contacting the workpiece, and high flexibility, induction brazing has a significant advantage over brazing the heat exchanger using a complex structure. In addition, induction heating is a highly efficient heating method for electrically conductive materials. During the induction brazing, resistance to the flow of electricity induced by coils placed around the workpiece provides the heat for the induction brazing process, and the heating is accomplished by generating eddy currents within the material when it is placed in an alternating magnetic field. The resistive, or Joule, losses created by the current cause the material to heat internally [7]. Therefore, the design of the coil has a significant influence on the control of the temperature field in the process of induction brazing.

Studies have shown that current parameters [8], coil shape [9–11], positional relationship between coil and workpiece [12], ferrite slices [13], and even the environmental characteristics [14] can significantly influence the temperature field on the workpiece. For example, Patil et al. [9] analyzed the magnetic fields and temperature control profiles of four different helical coils, including classical, conical, square, and oval coils, for tubular specimens; the results showed that the coil with the oval shape had the most uniform temperature distribution and the highest energy efficiency, at 62%. Ankan et al. [11] reviewed the matching relationships between the workpiece shapes and coil shapes, including single-turn coil, multi-turn coil, hairpin coil, and split coil, which are used for customized heating of work parts. However, the parameters of the coil should be designed according to the shape of the workpiece to obtain a suitable temperature field [15]. It is still difficult to choose the suitable coil due to the large number of parameters. To solve the multi-objective optimization problem under the condition of multi-factors, orthogonal experiments were usually designed and carried out, but the influence of accidental factors on the test results were often ignored; as a result, the optimal results were likely biased. In addition, artificial intelligence algorithms, such as machine learning, have been introduced to solve multi-factor optimization [16]. According to the research of Zhang et al. [17], the composition of precipitation-strengthened copper alloys was designed using machine learning, obtaining excellent combined mechanical and electrical properties, with the ultimate tensile strength of 858 MPa and electrical conductivity of 47.6% IACS. Liu et al. [18] proposed a material design strategy to simultaneously optimize multiple targeted properties of multi-component Co-based superalloys via machine learning, and a series of novel Co-based superalloys was successfully selected from more than 210,000 candidates. However, a large number of samples are needed to train the model during machine learning to ensure its accuracy.

To balance the accuracy and efficiency, the Taguchi method [19], a type of orthogonal experiment method which considers the influence of experimental noise, has often been

adopted [20]. Zhang et al. found that the optimum condition obtained from the Taguchi method to produce the maximum results was almost the same as that from the full factorial design via the comparison among the Taguchi method, orthogonal design, and full factorial design [21]. However, it is time-consuming and expensive to make different coils to carry out the brazing experiment. Thanks to the development of numerical simulation technology, commercial software has emerged to calculate the temperature distribution and stress distribution relevant to the physical process of brazing for the heat exchanger. In this study, a type of split coil was designed for the heat exchanger, and the Taguchi method was combined with multi-physical simulation to solve the multi-factor optimization problem. In addition, the simulation results were introduced into the Taguchi method with two noise factors to evaluate the feasibility of the split coil. Finally, the magnetic field, temperature field, stress field, and deformation during the induction brazing were evaluated under the optimized coil to clarify the mechanism of the successful brazing of three T-joints at one time.

2. Multi-Physical Simulation of Induction Brazing

2.1. The Principle of the Induction Brazing

Induction heating relies on two mechanisms of energy dissipation for heating, including Joule heating and energy losses. Joule heating is the sole mechanism of heat generation in nonmagnetic materials. During induction brazing, the magnetic field is generated by the alternating current on the surface of the coil; the alternating magnetic field induces an eddy current on the workpiece, and the eddy current results in the Joule heat. Additionally, the current distribution on the coil is affected by three special effects—ring effect, proximity effect, and boundary effect—and the depth of the current in the workpiece is called the skin depth because of the skin effect.

The skin effect can be described [6] by the following Formula (1). It depends on the material of the workpiece and the frequency of the current.

$$\Delta = \sqrt{\frac{1}{\pi f \mu \gamma}} \tag{1}$$

where f is the frequency of the current and μ and γ are the material properties of the workpiece, permeability and conductivity, respectively.

In the model, the mathematical relation among current, magnetic intensity, and Joule heat intensity can be described by Ampere's law and Faraday's law [9], which are shown in Formulas (2) and (3). In the model,

$$\nabla \times H = J + \frac{\partial D}{\partial t} \tag{2}$$

$$\nabla \times E = \frac{\partial B}{\partial t} \tag{3}$$

where H, E, D, B, and J denote the magnetic field intensity, the electric field intensity, the electric flux density, the magnetic flux density, and the conduction current density, respectively.

The transient heat transfer process in a workpiece can be described by the Fourier equation [9]:

$$c\gamma \frac{\partial T}{\partial t} + \nabla \cdot (-k \nabla T) = Q \tag{4}$$

where T, γ, c, and k denote the temperature, the density of the workpiece, the specific heat, and the thermal conductivity of the workpiece, respectively. In addition, Q is the heat source density per unit of time in a unit volume of the workpiece.

2.2. Finite Element Model

As shown in Figure 1, the heat exchanger was composed of header pipes, flat tubes, and round tubes, which were made of A3003, A1050, and A3003 aluminum alloy, respectively. What's more, the Al-Si solder (A4045) was adopted as the filler metal, which had been pre-coated on the surface of the header pipe with a thickness of 0.15 mm. The chemical compositions are listed in Table 1.

Table 1. Chemical Compositions of A1050/A3003/A4045.

Brand	Si	Fe	Cu	Mn	Mg	Zn	Ti	Al
A1050	0.25	0.40	0.05	0.05	0.05	0.05	0.03	Bal.
A3003	0.6	0.7	0.05	1.0	-	0.1	-	Bal.
A4045	10.0	0.8	0.3	0.05	0.05	0.10	0.2	Bal.

According to the feature heat exchanger in Figure 1b, many T-shaped joints need to be brazed at one time. A type of split coil was designed, as shown in Figure 2. Figure 2a depicts the relationship of the split coil and heat exchanger. The coil parameters and the positional relationship between the coil and workpiece are very important to the brazing. To obtain the optimal coil parameters, a technique flow chart was designed, as shown in Figure 2b. The multi-physical simulation was used to evaluate the influence of coil parameters on the temperature field. In addition, the properties of the material that was needed in the simulation model were provided by the JMatPro 7.0 software. Generally, the data provided by JMatPro software are the theoretical values of the material. To obtain relatively accurate data on the thermophysical parameters, they were calculated by the thermodynamic software JMatPro first, and then the actual parameters were tested and used to modify the calculated results. For example, the electrical resistivity of the specimen had a significant influence on the Joule heat, and it was obtained by the four-point technique whose principle and associated device are shown in Figure 2c; the result at room temperature was 3.856×10^{-8} $\Omega*$m, which is a little higher than the calculated result of 3.4×10^{-8} $\Omega*$m.
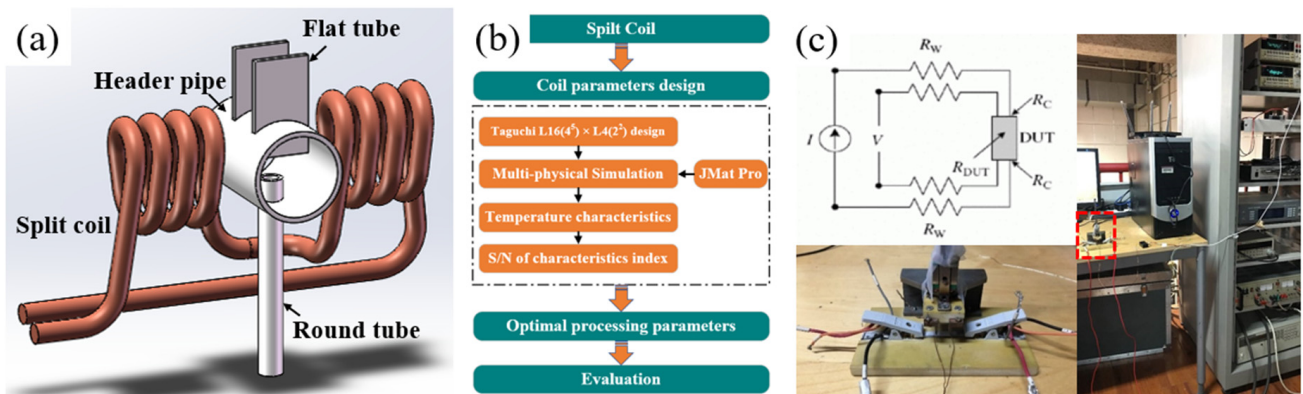
Figure 2. Induction brazing model: (**a**) split coil and workpiece, (**b**) the flow chart, and (**c**) the principle and device of the four-point technique.

Generally, the brazing process can be divided into three basic stages. First is the melting of the flux. With the increase in temperature, the present flux melts and enters into base metal clearance; this produces a physical and chemical reaction with the base metal oxide surface to remove the oxide film and clear the surface of the oxide film. Second, the filler metal melts and fills the brazing seam; in this model, the melting point of the filler metal was 563 °C. Third is the mutual reaction between the base metal and filler metal. Under the action of the molten solder, a small number of atoms of base metal will dissolve in the solder, while the filler metal experiences atomic diffusion into the base metal. A

complex chemical reaction occurs on the interface of solid and liquid. When temperature holds after a certain period, the solder fills the gap and then begins a cooling solidification and forms into the brazing joint. The simulation of filling the gaps is very time-consuming. Therefore, in this model, there are two main assumptions. One is that the melt and flow of the filler metal are ignored and the heat conductivity in the gaps will be set according to the temperature change during the brazing experiment. The other is that the metallurgical reaction heat between the filler metal and the base metal is ignored.

The brazing simulation model was established in ANSYS APDL software (R1 version). In this model, the direct coupling method was adopted. In other words, the magnetic field was calculated first, and then the Joule heat was applied as a heat source to the model when simulating the distribution of the temperature and stress fields of the brazing process. The element type was associated with the formulation type. Generally, there are three types of formulation. Nodal MVP and edge-based formulations were adapted to our model because the analysis type of our model was harmonic. Although an edge-based formulation has higher precision than a nodal MVP, an iron zone in the model is required when an edge-based formulation is used. As a result, in our model, the formulation type should be nodal MVP and the solid 97 should be chosen to analyze the magnetic field. As for the temperature field and stress field, the coupling element, Solid 5, will be used, as shown in Table 2.

Table 2. Element type and material properties in the region of induction heating.

Field	Electromagnetic Field		Temperature and Stress-Coupled Field	
	Element Type	Material Properties	Element Type	Material Properties
Flat tube	Solid 97	MURX, RSVX	Solid 5	KXX, DENS, C, ALPX, EX, PRXY
Round tube	Solid 97	MURX, RSVX	Solid 5	KXX, DENS, C, ALPX, EX, PRXY
Header pipe	Solid 97	MURX, RSVX	Solid 5	KXX, DENS, C, ALPX, EX, PRXY
Gap	Solid 97	MURX	Solid 5	KXX, DENS, C, ALPX, EX, PRXY
Coil	Solid 97	MURX, RSVX	Solid 5	None
Air	Solid 97	MURX	Solid 5	None

2.3. Experimental Design and Model Modification

The brazing experiment was finished on a platform, as shown in Figure 3, which consisted of an induction generator, controller cabinet, temperature controller, and split coil. The equipment model of the induction generator was SSF-50A2, whose current can be changed but which had a constant frequency. To obtain a suitable current value in the brazing experiment, the thermocouples were used to detect the distribution of the temperature field in the header pipe, and the current increased slowly until the filler metal was melted. As a result, a current of 365 A and a frequency of 32 kHz were chosen. During the experiment, the workpiece was laid flat on a ceramic substrate, which was used to prevent the heat from escaping. In addition, a ceramic block was put on the workpiece to prevent the workpiece from bouncing under the effect of electromagnetic force. There were also four thermocouples embedded into different places of the workpiece to monitor the temperature history during brazing.

The brazing simulation model and boundary condition are also shown in Figure 3. The mapping grid partitioning method was used to improve the convergence of calculation results, as shown in Figure 3d. Thermal boundary conditions had a very important effect on the temperature field in the model. Generally, the method of heat transference between the specimen and gas is radiation heat transfer and convective heat transfer. On the top and bottom of the header pipe, the contacting-heat-transfer boundary condition was applied, as in Figure 3e, due to the existence of the ceramic block (Figure 3b). In addition, there was an exhaust fan around the specimen; as a result, the radiation heat transfer was so low compared with the convective heat transfer that it could be ignored in the heating process. Therefore, in the model, the convective heat transfer coefficient was used to represent the level of heat transfer between the specimen and air.
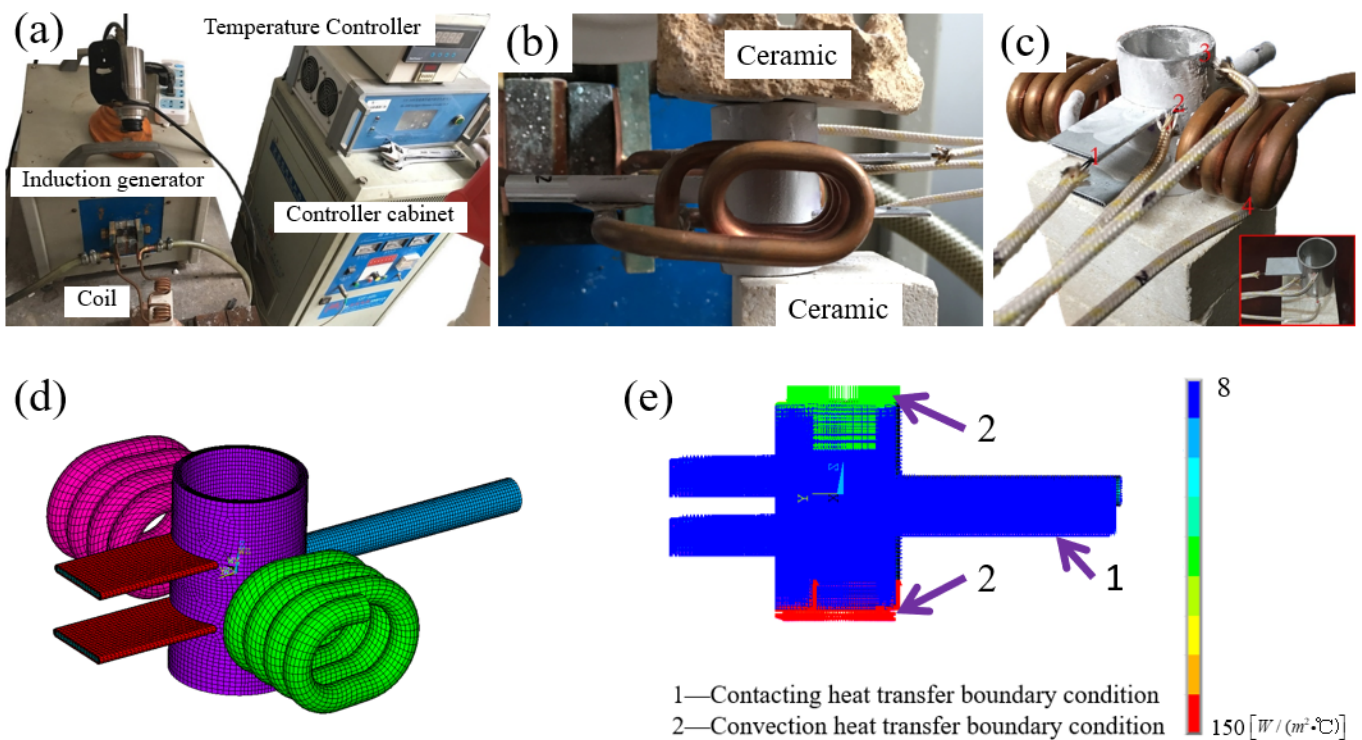
Figure 3. Brazing experiment platform and simulation model: (**a**) brazing equipment, (**b**) posture of workpiece, (**c**) distribution of thermocouples, (**d**) simulation model, and (**e**) boundary condition.

To modify the induction brazing model, a header pipe pre-coated with A4045 filler metal on the surface was chosen to carry out the induction brazing. A thermocouple welding machine was used to join the K type of the thermocouple to the header pipe, and the thermo-detector readings under different currents of the induction generator were obtained. The results of the temperature history of the simulation and experiment in Point 1 of the header pipe are illustrated in Figure 4a. The experimental results are shown as a solid line, and the maximum value of the temperature history is different when the current value is different. The simulation results are shown as dashed lines. It can easily be seen that the curve produced from the experiment almost coincides with that from the simulation, even when the maximum temperature in Point 1 is different. The average error of the simulation results was approximately 5.753 °C when the maximum heating temperature was 570 °C. That means that the 3D model was reliable. To further evaluate this model, the temperature field and the filler metal condition were compared, as seen in Figure 4b. It can be noted that the non-molten filler metal (Zone A) has the same shape with a temperature field below 563 °C (Zone B), which is the molten point of the filler metal. Therefore, the results of the simulation are plausible.
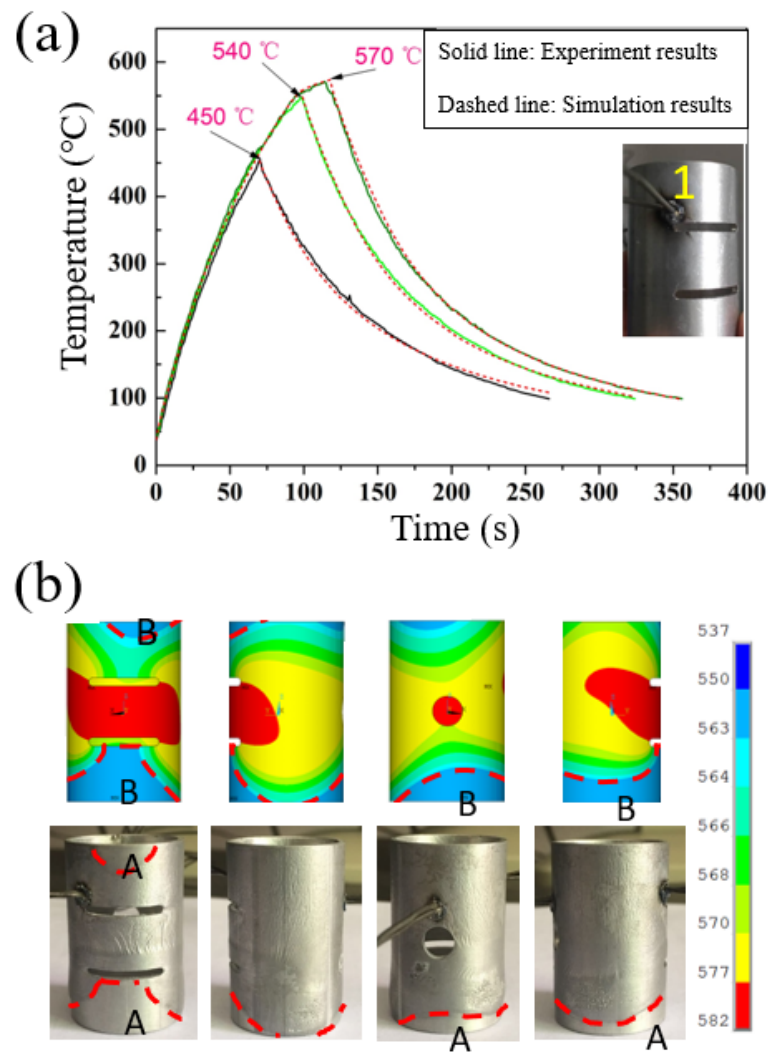
Figure 4. Model validation and modification: (**a**) the comparison of experimental and simulation temperature histories under different brazing parameters and (**b**) the temperature field on the header pipe and distribution of the melting filler metal on the surface of the header pipe.

3. Coil Parameters Design

The melting point difference between the header pipe (A3003) and the Al-Si filler metal (A4045) was less than 50 °C; as a result, the component was likely to melt first compared with the filler metal due to the uneven temperature field caused by the induction generator. Therefore, the design of the coil was very important in obtaining a uniform temperature field on the header pipe. The distribution of the temperature field depended mainly on the shape of the coil. In addition, the size, shape, contour, number of turns, and turn spacing of the coil all affected the strength of the electromagnetic field and the heat pattern. As a result, it was difficult to determine the best parameter combination from so many parameters. Therefore, the Taguchi method, a type of orthogonal experimental design, was engaged. As far as we have considered, the number of turns, the space of turn, the heating distance, the diameter of the coil, and the length of the coil, as shown in Figures 5 and 6, are the five most important coil parameters. Thus, the induction brazing model was used to discuss the influence of these parameters on the temperature field and to obtain the optimal parameters.
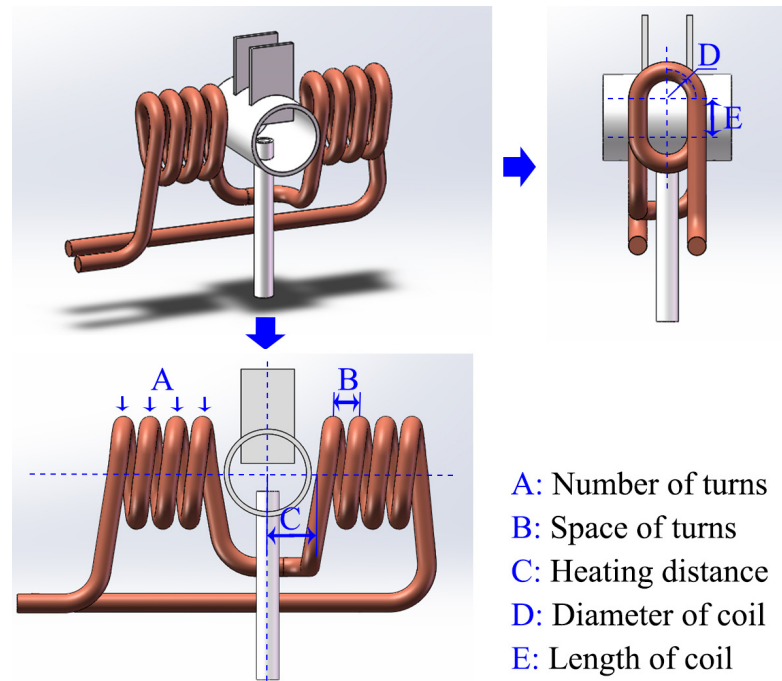
Figure 5. Coil parameter design.

A: Number of turns
B: Space of turns
C: Heating distance
D: Diameter of coil
E: Length of coil
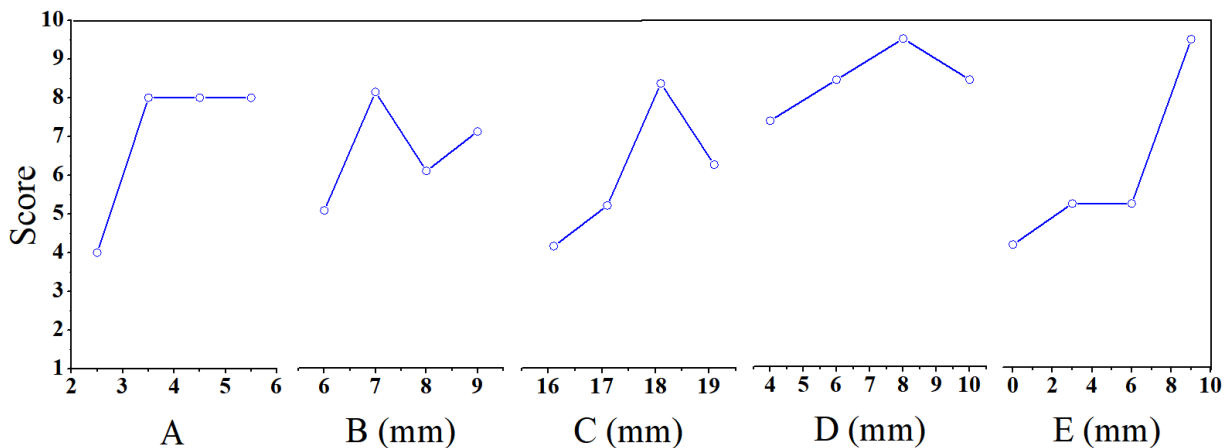
Figure 6. The comprehensive scores of the coil parameters.

On the basis of the Taguchi method, the heating experiments were designed to explore the optimum coil parameters. The minimum temperature on the header pipe was used to evaluate inductors for coil efficiency and temperature field distribution. In the Taguchi method, the ratio of signal to noise (S/N), as a robust indicator of output characteristics, was used to reduce the influence of uncontrollable factors (or named deviation) on the desired target. Generally, for engineering analysis, S/N of the quality characteristics can be divided into three types:

1. Larger-the-better (for example, production output);
2. Smaller-the-better (for example, carbon emissions);
3. On-target, minimum-variation (for example, a mating part in an assembly).

During the simulation, the header pipe will be heated to 600 °C (the maximum temperature) with different coil. Furtherly, the minimum temperature of the header pipe is higher, the distribution of temperature on the header pipe is more uniform. Therefore, the value of minimum temperature (T_{min}) of the header pipe is chosen to evaluate the influence

of the coil and a smaller-the-better S/N is appropriate. A smaller-the-better S/N (S/N_S) can be calculated by Formula (5):

$$S/N_S = -10 \times \lg \left(\frac{1}{n} \sum_{i=1}^{n} y_i^2 \right) \tag{5}$$

where y_i is the output characteristic value of the ith sample and n is the total number of samples.

In this study, five main factors and their corresponding levels were chosen and are listed in Table 3; the levels of noise factors also were considered and are shown in Table 4. In the Taguchi experiment, the number of turns A, the space of turn B, heating distance C, the diameter of coil D, and the length of coil E were set to 2.5–5.5, 6–9, 16.1–19.1, 4–10, and 0–9, respectively. All the factors were set to four levels because of possible nonlinear influence. According to the orthogonal design, to obtain the optimal coil parameters, 16 groups of parameters, including the control factor and noise factor, needed to be generated via simulation, as shown in Table 5. In addition, the y_{ij} was the scoring of the coil with the parameters in the ith group of the control factor and the jth group of the noise factor, and the scoring of every group was the average of y_{i1}, y_{i2}, y_{i3}, and y_{i4}.

Table 3. Levels of the control factors.

Influential Factor	Unit	Factor Level			
		Level 1	Level 2	Level 3	Level 4
A. Number of turns		2.5	3.5	4.5	5.5
B. Space of turn	mm	6	7	8	9
C. Heating distance	mm	16.1	17.1	18.1	19.1
D. Diameter of coil	mm	4	6	8	10
E. Length of coil	mm	0	3	6	9

Table 4. Levels of the noise factors.

Influential Factor	Unit	Symbol	Factor Level	
			Level 1	Level 2
A. Lateral deviation	mm	ΔLA	0	±0.5
B. Longitudinal deviation	mm	ΔLO	0	±0.5

Table 5. L16 (4^5) × L4 (2^2) orthogonal array.

Orthogonal Table Type		Inner Orthogonal Array L$_{16}$ (4^5)					External Orthogonal Array L$_4$ (2^2)				
Factor		Control factor					Noise Factor				
							Exp. order				Arrangement
							S11	S12	S21	S22	
Exp. Order	Column	A	B	C	D	E	1	1	2	2	U
							1	2	1	2	V
1		1	1	1	1	1	$y11$	$y12$	$y13$	$y14$	
2		1	2	2	2	2	$y21$	$y22$	$y23$	$y24$	
3		1	3	3	3	3	$y31$	$y32$	$y33$	$y34$	
4		1	4	4	4	4	$y41$	$y42$	$y43$	$y44$	
5		2	1	2	3	4	$y51$	$y52$	$y53$	$y54$	
6		2	2	1	4	3	$y61$	$y62$	$y63$	$y64$	
7		2	3	4	1	2	$y71$	$y72$	$y73$	$y74$	
8		2	4	3	2	1	$y81$	$y82$	$y83$	$y84$	

Table 5. *Cont.*

Orthogonal Table Type	Inner Orthogonal Array L$_{16}$ (4^5)					External Orthogonal Array L$_4$ (2^2)				
						Noise Factor				
Factor	**Control factor**					Exp. order				Arrangement
						S11	S12	S21	S22	
Column	A	B	C	D	E	1	1	2	2	U
Exp. Order						1	2	1	2	V
9	3	1	3	4	2	$y91$	$y92$	$y93$	$y94$	
10	3	2	4	3	1	$y101$	$y102$	$y103$	$y104$	
11	3	3	1	2	4	$y111$	$y112$	$y113$	$y114$	
12	3	4	2	1	3	$y121$	$y122$	$y123$	$y124$	
13	4	1	4	2	3	$y131$	$y132$	$y133$	$y134$	
14	4	2	3	1	4	$y141$	$y142$	$y143$	$y144$	
15	4	3	2	4	1	$y151$	$y152$	$y153$	$y154$	
16	4	4	1	3	2	$y161$	$y162$	$y163$	$y164$	

To evaluate the effect of different parameters, a scale of 1 to 10 was created for each of the results, and we assigned each result a score within this range from two sides (magnetic field and temperature field). In addition, the principles of the scoring are listed as follows:

(a) The magnetic intensity around the joint is stronger, and the score is higher.
(b) The distribution of the magnetic field on both the round tube and the flat tube is more uniform, and the score is higher.
(c) The temperature value on the flat tube is lower, and the score is higher.
(d) The temperature field is more important than the magnetic field. Therefore, the magnetic field is defined as 40 percent of the full mark, and the temperature field is defined as 60 percent of the full mark.

The detailed scoring regulations and rules are listed in Table 6.

Table 6. Detailed scoring regulations and rules.

Classification	Magnetic Field Intensity around the Joint and Distribution near the Flat Tube and Round Tube				Minimum Temperature on Header Pipe/°C					
Score	1	2	3	4	1	2	3	4	5	6
Content	High and uniform	Higher and more uniform	Higher and most uniform	Highest and most uniform	<573	573–580	580–585	585–590	590–595	595–600

According to the results of the Taguchi method, when A was 3.5, B was 7 mm, C was 15.6 mm, D was 8 mm, and E was 9 mm, a uniform temperature field could be achieved.

4. Simulation and Experimental Results

4.1. Magnetic Field

Figure 7 shows the distribution of the current density on the coil and the induced magnetic field around the split coil. According to the main view and left view Figure 7a, the high current density area was located mainly on the inside of the induction coil and the adjacent surface of two turns of the coil. It is worth noting that the current density on the inside of the coil was almost twice as high as that on the outside. The distribution of the current density on the coil was substantially consistent with the three effects, specifically, proximity effects, ring effects, and skin effects. According to Lenz's law, the eddy current was created inside the coil in the opposite direction of the current in the coil, causing the electromotive force at the center of the coil to be greater than the electromotive force at the surface; as a result, the current flowed only on the surface of the coil. The distribution of the current on the surface of the coil had a significant relationship with the magnetic field. The distribution of the magnetic field induced by the coil is shown in Figure 7b, where the

current in the same direction and magnitude was applied to the two coils. The magnetic field was always more dispersed outside the coil, which caused the current outside the coil to pass through more magnetic fields than the current inside. This created an alternating back electromotive force, making the potential outside the coil less than the potential inside, causing the current density outside the coil to be less than the current inside the coil. In addition, it is easy to see that the magnetic field lines are mainly around the coil, as shown by the arrows in Figure 7b. Although the distance between the two coils was large, there were still a few magnetic field lines entering into the other coil.
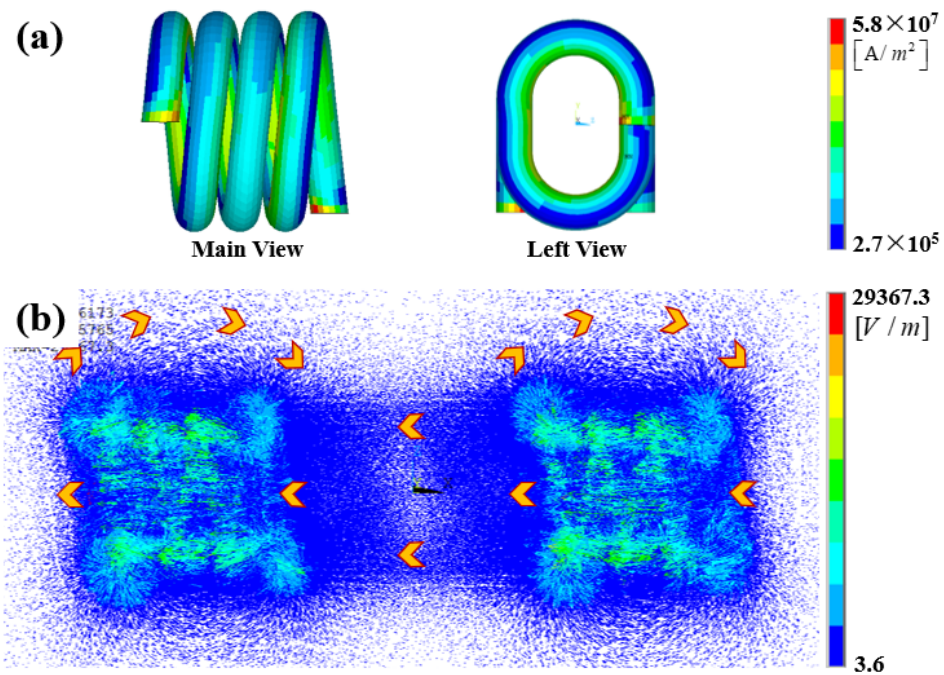
Figure 7. The magnetic field characteristics of the split coil. (**a**) The contour map of the current density on the coil and (**b**) the vector diagram of the magnetic field induced by the coil.

The distribution of the magnetic field during the induction brazing is shown in Figure 8. According to Figure 8a, the distribution of the magnetic field on the workpiece was significantly uneven and the magnetic field intensity near the center of the coil was larger than in other locations due to the strong magnetic flux in the center of the coil. Compared with Figure 7b, a great deal of magnetic field was produced around the sample, especially on the header pipe, as Figure 8b shows. In addition, quite a lot of magnet flux was produced in the gap between the flat tube and round tube, which means the gap was heated during the induction brazing. According to Figure 8c, the magnetic flux in the gaps had a significant relationship with the length of the coil and the diameter of the coil.

Figure 9 illustrates the distribution of the eddy current density and Joule heat induced by the magnetic field. It can be seen from the image that the shape of the eddy current field was similar to the coil, and the eddy current density focused mainly on the surface of the header pipe. It is worth noting that the shape of the eddy current field did not coincide with the shape of the magnetic field strength on the workpiece. This shows that the distance between the workpiece and the coil was a key factor affecting the shape and strength of the eddy current field. Moreover, there was a high eddy current density around the joint, which indicates that the gap was prone to producing high eddy current density (Figure 9b). Alternating magnetic fields produce alternating electric fields. Therefore, the high eddy current density likely had a relationship with the high magnetic field intensity, which was affected mainly by coil length and coil diameter. As a result, the Joule heat in the joints was higher (Figure 9c) which was very advantageous to the melting and filling of the solder in the joint position.
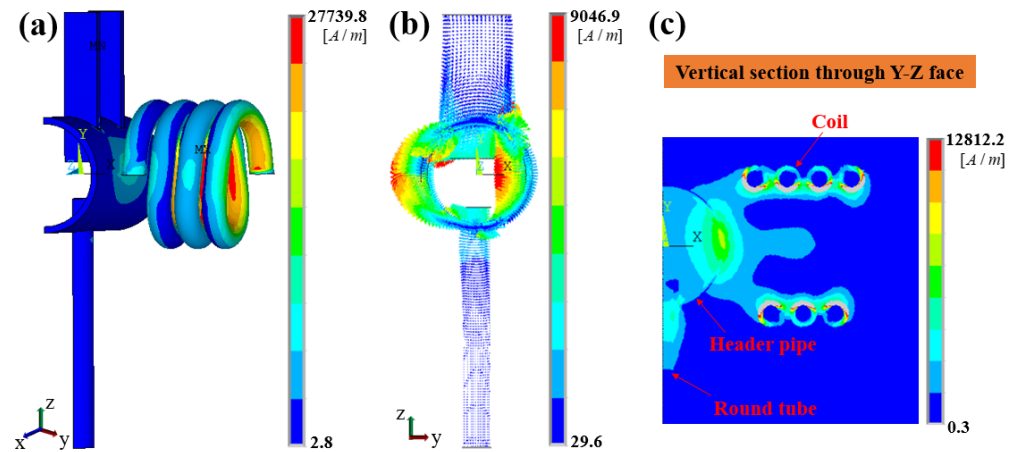
Figure 8. The magnetic field characteristics during induction brazing: (**a**) the contour map of the magnetic field on the component and coil, (**b**) the vector diagram of the magnetic field on the component, and (**c**) the magnetic field on the vertical section through the Y-Z face.
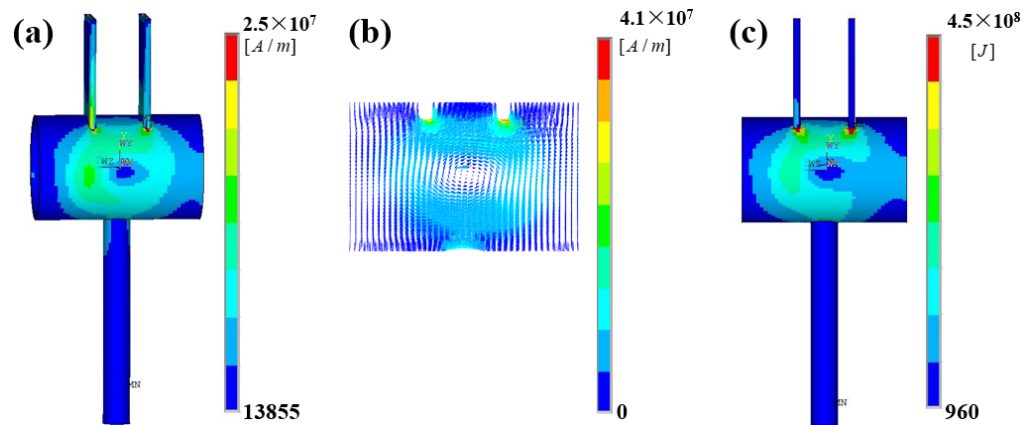
Figure 9. Other fields induced by the magnetic field: (**a**) the contour map of the eddy current density on the component, (**b**) the vector diagram of eddy current density on the header pipe, and (**c**) the contour map of the Joule heat on the component.

4.2. Temperature Field and Deformation

Figure 10 shows the joints using induction brazing technology. From the enlarged part of the joint in Figure 10b, it can easily be seen that the joints had a good formation, and all three joints are formed. Figure 10c provides the microstructure of the brazing joint. All the joints are filled with filler metal; however, the fillets on two sides of the joint are different because of the effect of gravity, and in the joint, there are a few holes. In addition, there was quite a lot of residual filler metal on the surface of the header pipe; however, when the soaking time was too long, the melted filler metal gathered and became a welding tumor on the bottom of the header pipe. From the cross-section picture in Figure 10c, the base metal was scarcely melted.
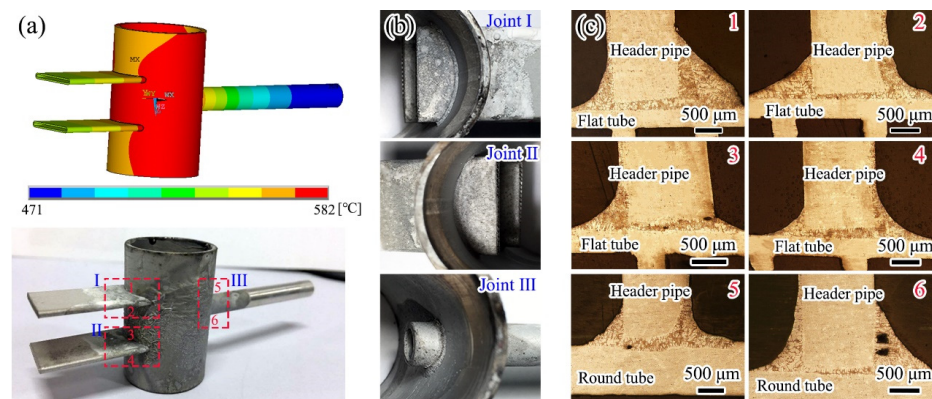
Figure 10. The induction brazing experiment: (**a**) temperature field at the end of the heating process and the induction brazing component, (**b**) morphologies of the joints in different positions, and (**c**) microstructure of the joints in different positions.

On the brazing specimen, two feature points were chosen, and their temperature histories are shown in Figure 11. Since Point B was less affected by the magnetic field (Figure 8), most of the heat at Point B came from the collecting pipe, so the thermal cycle curves at the two points were very similar in shape. During the heating process, the temperature rose very quickly, and then the speed became very slow when the temperature was approximately 560 °C; this illustrates the benefit of keeping the temperature of the header pipe under its melting point, which also helped to make the distribution of the temperature more uniform. During the cooling process, the two curves in Figure 11 are almost coincident, which means the temperature on the flat tube and header pipe was uniform during that time. In addition, the flat tube in Figure 11 had its lowest temperature during the heating process; however, the time during which the temperature was higher than 200 degrees lasted as long as 239 s, which could have a bad effect on the joint between the flat tube and fins. Therefore, to successfully apply this type of coil to the connection of the header pipe, round tube, and flat tube in the heat exchanger, on the one hand, the distance between the fin (Figure 1a) and header tube should be increased; on the other hand, one side of the fin can be cooled to avoid the failure of the adhesive joint between fins and the flat tube caused by the high temperature. Figure 11b shows the deformation curve along the length of Point B in the process of brazing. In the process of brazing, the maximum deformation of Point B was approximately 0.33 mm, and the deformation after welding was approximately 0.036 mm. Deformation had little effect on the heat exchanger. By comparing Figures 9a and 11b, it can be seen that the deformation curve of Point B is very close to its thermal cycle curve in shape. This indicates that the deformation of flat tubes is due mainly to the action of heat.

The split coil with optimal parameters has a great advantage in production automation because of its structure. When the coil is in operation, it can slowly move along the length direction of the header pipe; additionally, it is easy to automate the connection of the T-joints on the header pipe, which is very helpful in improving production efficiency. However, there are still two important avenues to investigate to make the split coil better serve production in the future. Firstly, it is necessary to explore the solution of restraining the excessive temperature on the fin, and secondly, it is necessary to explore the temperature field management process during the movement of the split coil.
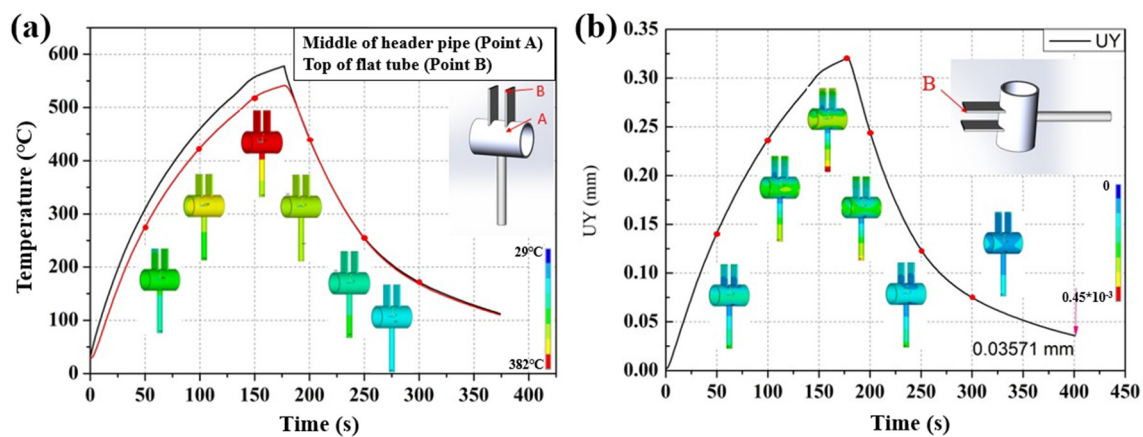
Figure 11. Simulation results: (**a**) temperature history in feature points and (**b**) deformation history in the feature point.

5. Conclusions

In this paper, commercial software ANSYS and ANSYS Multiphysics modules were used to simulate numerically the effect of split coils on the induction brazing process of T-shaped aluminum alloy joints and optimize the split coil parameters. Brazing experiments were conducted to verify the results, and the main conclusions are as follows:

(1) A multi-physical simulation model with high precision was established. The melting of filler metal was almost consistent with the spatial distribution of the temperature field, and the temperature history in the header pipe could be consistent with the experimental results under different brazing parameters. The average simulation error was approximately 5.753 °C.

(2) The Taguchi method was combined with multi-physical simulation to solve the multi-factor optimization problem. The optimal coil parameters were obtained with a turn number of 3.5, a turn space of 7 mm, a heating distance of 15.6 mm, a coil diameter of 8 mm, and a coil length of 9 mm. Three well-formed T-shaped joints could be obtained at one time via the optimal split coil.

(3) The mechanism of a good joint form was clarified. The reason for the good joints lay in the significant decrease in the heating rate at high temperatures, which promoted the homogenization of the temperature and the melting and filling of the filler metal as well as avoided local overheating.

(4) The relationship between the coil and the temperature field was clarified. The skin effects and the proximity effects induced a high magnetic field intensity around the joint, which had a significant relationship with the length of the coil and the diameter of the coil. The high magnetic field intensity promoted a high eddy current density in this place. As a result, the high Joule heat could be generated around the joint.

Author Contributions: Conceptualization, J.S. and A.W.; methodology, Z.Z.; software, Z.Z. and P.X.; validation, Z.Z.; formal analysis, Z.Y. and S.M.; investigation, Z.Y. and L.Z.; resources, Z.Z. and H.C.; data curation, Y.L. and Y.Z.; writing—original draft preparation, Z.Z.; writing—review and editing, Z.Z.; visualization, Z.Z. and Z.Y.; supervision, H.C.; project administration, J.S.; funding acquisition, Z.Z. All authors have read and agreed to the published version of the manuscript.

Institutional Review Board Statement: Not applicable.

Informed Consent Statement: Not applicable.

Data Availability Statement: The raw/processed data required to reproduce these findings are available from the corresponding author upon reasonable request.

Conflicts of Interest: The authors declare no conflict of interest.

References

1. Irabatti, V.; Patil, Y.; Kore, S.; Barangule, V.; Kothe, A. Comprehensive review of spiral heat exchanger for diverse applications. *Mater. Today Proc.* **2023**, *72*, 1328–1334. [CrossRef]
2. Li, N.; Klemeš, J.J.; Sunden, B.; Wu, Z.; Wang, Q.; Zeng, M. Heat exchanger network synthesis considering detailed thermal-hydraulic performance: Methods and perspectives. *Renew. Sustain. Energy Rev.* **2022**, *168*, 112810. [CrossRef]
3. Dai, W.; Xue, S.-B.; Lou, J.-Y.; Lou, Y.-B.; Wang, S.-Q. Torch brazing 3003 aluminum alloy with Zn—Al filler metal. *Trans. Nonferrous Met. Soc. China* **2012**, *22*, 30–35. [CrossRef]
4. Yu, W.-Y.; Zhang, T.-Y.; Wang, Y.; Gao, M.-Z.; Shang, J.-X.; Yan, Z.-H.; Wu, W.-J.; Lin, Q.-L. Formation and elimination of burst phenomenon in ultrasonic-assisted resistance brazing. *Trans. Nonferrous Met. Soc. China* **2019**, *29*, 485–494. [CrossRef]
5. Zhang, X.; Li, D.; Wang, L.; Wan, C.; Song, L.; Song, K.; Xiao, Y. Ultrasonic brazing of Zr-based bulk metallic glass and 1060 Al alloy using Zn-3Al filler metal. *J. Adv. Join. Process.* **2022**, *5*, 100095. [CrossRef]
6. Nian, S.C.; Tsai, S.W.; Huang, M.S.; Huang, R.C.; Chen, C.H. Key parameters and optimal design of a single-layered induction coil for external rapid mold surface heating. *Int. Commun. Heat Mass Transf.* **2014**, *57*, 109–117. [CrossRef]
7. Zhang, L. Filler metals, brazing processing and reliability for diamond tools brazing: A review. *J. Manuf. Process.* **2021**, *66*, 651–668. [CrossRef]
8. Prasad, A.K.; Kapil, S.; Bag, S. Critical conditions for melting of metallic wire in induction heating system through numerical simulation and experiments. *J. Manuf. Process.* **2022**, *77*, 678–693. [CrossRef]
9. Patil, M.; Choubey, R.K.; Jain, P.K. Influence of coil shapes on temperature distribution in induction heating process. *Mater. Today Proc.* **2023**, *72*, 3029–3035. [CrossRef]
10. Heidari, H.; Tavakoli, M.H.; Shokri, A.; Moradi, B.M.; Sharifi, O.M.; Asaad, M.J.M. 3D simulation of the coil geometry effect on the induction heating process in Czochralski crystal growth system. *Cryst. Res. Technol.* **2020**, *55*, 1900147. [CrossRef]
11. Mishra, A.; Bag, S.; Pal, S. Induction Heating in Sustainable Manufacturing and Material Processing Technologies-A State of the Art Literature Review. In *Reference Module in Materials Science and Materials Engineering*; Elsevier: Amsterdam, The Netherlands, 2020; Volume 1, pp. 343–357.
12. Sung, Y.-T.; Hwang, S.-J.; Lee, H.-H.; Huang, D.-Y. Study on Induction Heating Coil for Uniform Mold Cavity Surface Heating. *Adv. Mech. Eng.* **2014**, *6*, 349078. [CrossRef]
13. Nian, S.; Huang, M.; Tsai, T. Enhancement of induction heating efficiency on injection mold surface using a novel magnetic shielding method. *Int. Commun. Heat Mass Transf.* **2014**, *50*, 52–60. [CrossRef]
14. Kim, M.; Youn, B.; Bullard, C.W. Effect of inclination on the air-side performance of a brazed aluminum heat exchanger under dry and wet conditions. *Int. J. Heat Mass Transf.* **2001**, *44*, 4613–4623. [CrossRef]
15. Wen, H.; Han, Y. Study on mobile induction heating process of internal gear rings for wind power generation. *Appl. Therm. Eng.* **2017**, *112*, 507–515. [CrossRef]
16. Fang, J.; Xie, M.; He, X.; Zhang, J.; Hu, J.; Chen, Y.; Yang, Y.; Jin, Q. Machine learning accelerates the materials discovery. *Mater. Today Commun.* **2022**, *33*, 104900. [CrossRef]
17. Zhang, H.; Fu, H.; Zhu, S.; Yong, W.; Xie, J. Machine learning assisted composition effective design for precipitation strengthened copper alloys. *Acta Mater.* **2021**, *215*, 117118. [CrossRef]
18. Liu, P.; Huang, H.; Antonov, S.; Wen, C.; Xue, D.; Chen, H.; Li, L.; Feng, Q.; Omori, T.; Su, Y. Machine learning assisted design of γ'-strengthened Co-base superalloys with multi-performance optimization. *Npj Comput. Mater.* **2020**, *6*, 62. [CrossRef]
19. Taguchi, G.; Chowdhury, S. *Robust Engineering: Learn How to Boost Quality While Reducing Costs & Time to Market*; Mcgraw Hill Book Co.: New York, NY, USA, 1999; Volume 70.
20. Aman, A.; Bhardwaj, R.; Gahlot, P.; Phanden, R.K. Selection of cutting tool for desired surface finish in milling Machine using Taguchi optimization methodology. *Mater. Today Proc.* **2023**, *78*, 444–448. [CrossRef]
21. Zhang, F.; Yang, M.; Li, Z. Feasibility analysis of replacing full factorial design with Taguchi method in mini-plot soil erosion experiments. *Trans. Chin. Soc. Agric. Eng.* **2015**, *31*, 1–9.